Fe-doping effects on the structural, vibrational, magnetic, and electronic properties of ceria nanoparticles

Fermin F. H. Aragón, Juan C. R. Aquino, Jesus E. Ramos, José A. H. Coaquira, Ismael Gonzalez, Waldemar A. A. Macedo, Sebastião W. da Silva, and Paulo C. Morais

Citation: Journal of Applied Physics **122**, 204302 (2017);
View online: https://doi.org/10.1063/1.4999457
View Table of Contents: http://aip.scitation.org/toc/jap/122/20
Published by the American Institute of Physics

Fe-doping effects on the structural, vibrational, magnetic, and electronic properties of ceria nanoparticles

Fermin F. H. Aragón,[1] Juan C. R. Aquino,[1] Jesus E. Ramos,[1] José A. H. Coaquira,[1] Ismael Gonzalez,[2] Waldemar A. A. Macedo,[2] Sebastião W. da Silva,[1] and Paulo C. Morais[1,3]

[1]*Núcleo de Física Aplicada, Instituto de Física, Universidade de Brasília, 70910900 Brasília, DF, Brazil*
[2]*Centro de Desenvolvimento da Tecnologia Nuclear, CDTN, 31270-901 Belo Horizonte, MG, Brazil*
[3]*School of Chemistry and Chemical Engineering, Anhui University, Hefei 230601, China*

(Received 8 August 2017; accepted 6 November 2017; published online 27 November 2017)

In this work, we report on a single-pot synthesis route based on a polymeric precursor method used for successfully producing undoped and iron-doped CeO_2 nanoparticles with iron contents up to 10.0 mol. %. The formation of high-crystalline nanoparticles with a cubic fluorite structure is determined for all the studied samples. Meanwhile, the magnetic measurements of the undoped ceria nanoparticles revealed the occurrence of ferromagnetism of bound magnetic polarons of a fraction of Ce^{3+} at room temperature, and only a paramagnetic behavior of Fe^{3+} ions was determined for Fe-doped ceria nanoparticles. A monotonous reduction of the effective magnetic moment of the Fe^{3+} ions was determined. It suggests a change from a high-spin to low-spin state of Fe ions as the Fe content is increased. The 3+ valence state of the iron ions has been confirmed by the Fe K-edge X-ray absorption near-edge structure (XANES) and Mössbauer spectroscopy measurements. X-ray photoelectron spectroscopy data analysis evidenced a coexistence of Ce^{3+} and Ce^{4+} ions and a decreasing tendency of the relative fraction of Ce^{3+} ions in the surface region of the particles as the iron content is increased. Although the coexistence of Ce^{3+} and Ce^{4+} is confirmed by results obtained via Ce L_3-edge XANES measurements, any clear dependence of the relative relation of Ce^{3+} ions on the iron content is determined, suggesting a homogeneous distribution of Ce^{3+} and Ce^{4+}-ions in the whole volume of the particles. Ce L_3-edge extended X-ray absorption fine structure revealed that the Ce-O bond distance shows a monotonous decrease as the Fe content is increased, which is in good agreement with the shrinking of the unit cell volume with the iron content determined from XRD data analysis, reinforcing the substitutional solution of Ce and Fe ions in the CeO_2 matrix. *Published by AIP Publishing*. https://doi.org/10.1063/1.4999457

INTRODUCTION

There is a growing interest in lanthanide oxides in recent years, particularly in regard to ceria (CeO_2) due to its wide range of applications in oxygen storage in three-way catalytic converters for gasoline exhausting gas cleanup,[1–3] resistance random access memories (ReRAM),[4] gas sensors,[5] and direct oxidation of hydrocarbons in solid oxide fuel cells for electrical power generation.[6] The ultraviolet-visible (uv-vis) absorption characteristics and the oxygen ion sorption-desorption capability are enhanced in low-dimensional ceria counterparts (including nanoparticles, thin films, nanotubes, and nanorods) because of a drastic increase in the surface-to-volume ratio under size reduction. Due to symmetry breaking at the nanoparticle (NP) surface plus reduced surface coordination number, the presence of oxygen vacancy (Vo) is expected, which can provide localized or delocalized electron states, thus introducing ferromagnetic (FM) properties into the system likely mediated by electrons trapped in the Vo (F-centers).[7,8] These findings are consistent with those reported by Sundaresan *et al.*,[9] which stated that ferromagnetism is a universal phenomenon in particles of extremely small sizes. However, when the size of ceria particles is reduced down to the nanosize range, the onset of defects related to broken bonds and symmetry breaking leads to the presence of Ce^{3+}-ions,[10] which have nonzero magnetic moment ($4f^1$). On the other hand, the doping process with small amounts of magnetic elements, such as transition metal (TM) or rare earth (RE) elements, having partially filled *d*- or *f*-shells, can provide a new degree of freedom to the system, driving to the so-called oxide diluted magnetic semiconductors (ODMS). Moreover, the ODMS may exhibit high-temperature ferromagnetism,[11,12] which is interesting for technological applications, such as in spintronics devices and magnetic gas sensors.[13] However, the origin of ferromagnetism in ODMS is not yet well understood and it is still on debate, leading to controversies, which are mainly related to the role played by the dopant ions and the poor reproducibility of the experimental data. As mentioned earlier, while in the nanosize range, ceria may show the coexistence of Ce^{4+}- and Ce^{3+}-ions, adding additional magnetic contribution to the system credited to the nonzero magnetic moment of Ce^{3+}-ions. Therefore, the establishment of robust synthesis routes for undoped and TM-doped/RE-doped ceria NPs, owing to fabricate high-quality and single phase end products, is a pre-condition to push forward with the understanding of related fundamental issues, such as ferromagnetic ordering in ODMS. Based on a comprehensive and reliable material platform, breakthrough in technological applications shall emerge naturally. In this regard, we are herein

reporting on a successful route of production of high-quality ceria NPs using a single-pot protocol based on a polymeric precursor method, which is indeed ease of scaling up. Additionally, the same protocol was successfully used to produce high-quality iron-doped ceria NPs in a fairly wide range of doping (0–10 mol. %). The high quality of the as-produced undoped and iron-doped ceria NPs was assesses via thermal, morphological, structural, vibrational, magnetic, and electronic properties. Thermogravimetric analysis (TGA), X-ray diffraction (XRD), high-resolution transmission electron microscopy (HRTEM), Raman spectroscopy, magnetic measurements, X-ray photoelectron spectroscopy (XPS), X-ray absorption near edge structure (XANES), and extended X-ray absorption fine structure (EXAFS) were used to support the claim of high-quality as-produced samples and to assess information about the effects of the iron doping.

EXPERIMENTAL DETAILS

Iron-doped ceria NPs with Fe-content up to 10 mol. % was synthesized by a polymeric precursor method.[14] In short, the synthesis of undoped ceria NPs started with an initial solution prepared by mixing 26.6 wt. % of cerium nitrate [$Ce(NO_3)_3{\cdot}2H_2O$], 47.7 wt. % of citric acid ($C_6H_8O_7$), and 31.7 wt. % of ethylene glycol ($C_2H_6O_2$). The obtained solution was heated to 180–200 °C to promote polymerization of citric acid and ethylene glycol, which resulted in the formation of a polymer backbone with sites available to react with metallic ions (Ce^{3+} and Fe^{3+}). Next, the obtained liquid precursor was thermally treated at 400 °C (4 h) to produce a dry carbon-rich powder, followed by grinding and treating at 500 °C (15 h) to warrant a single-phase formation and good crystallinity. Following the same synthesis protocol, ferric nitrate [$Fe(NO_3)_3{\cdot}9H_2O$] was used to synthesize iron-doped ceria NPs with the Fe content controlled according to the atomic relation: Fe/(Fe + Ce). XRD patterns were recorded using a commercial diffractometer equipped (Rigaku, model Ultima IV) with a CuKα (1.5418 Å) radiation source. The lattice constant and the average crystallite size were assessed from the XRD data analysis using the Rietveld refinement method (DBWS program).[15] The shape of the XRD peaks was modeled using the Thompson-Cox-Hastings pseudo-Voigt function,[16] which allowed deconvolution of the total full width at half maximum (FWHM) for Gaussian (Γ_G) and Lorentzian (Γ_L) components. The experimental data correction from the instrumental contribution was obtained via a standard Si single crystal. Both Γ_{size} and Γ_{strain} were calculated using the relation: $\Gamma = (\Gamma_G^5 + A\Gamma_G^4\Gamma_L + B\Gamma_G^3\Gamma_L^2 + C\Gamma_G^2\Gamma_L^3 + D\Gamma_G\Gamma_L^4 + \Gamma_L^5)^{0.5}$, where A = 2.69269, B = 2.42843, C = 4.47163, and D = 0.07842.[16] The mean crystallite size $\langle D \rangle$ and the mean residual strain $\langle \varepsilon \rangle$ were obtained from the standard relations $\langle D \rangle = K\lambda/(\Gamma_{size}\cos\theta)$ and $\langle \varepsilon \rangle = \frac{\Gamma_{strain}}{4\,\mathrm{tg}\theta}$, respectively.[17] The magnetic measurements were carried out using a vibrating sample magnetometer (VSM) module of a physical property measurements system (PPMS, Quantum Design, Inc.). The scanning of the applied field was done in the ±5 kOe range, and the temperature was varied from 5 to 300 K. Mössbauer spectra were recorded at room temperature (RT) and 20 K, in the 10 mol. % iron doped ceria, using the ^{57}Co radioactive source. A α-Fe foil was used as reference for the isomer shift, and all Mössbauer spectra were fitted with the least-square fitting routine using the NORMOS program. Raman spectra were obtained using the 532 nm line of an Ar^+-laser beam, focused by a spherical lens. The scattered photons were dispersed using a commercial triple spectrometer (Jobin Yvon, T64000) and detected with a liquid-nitrogen-cooled charge-coupled device. HRTEM images were recorded using a JEOL system (model JEM-2100). XPS analysis was done using a SPECS surface analysis system equipped with a Phoibos 150 electron analyzer, using a monochromatic AlKα radiation (1486.6 eV), with output power set at 350 W. To collect the high-resolution XPS spectra, the pass-energy was set at 30 eV with a step of 0.1 eV. The *C*(1s) signal (284.6 eV) was employed as reference for calibration of the binding energy (BE) of different elements in order to correct the charge effect. The CasaXPS software was used to process all XPS data and to estimate the sample surface atomic concentration. In order to study the electronic and atomic structures, X-ray absorption spectroscopy (XAS) measurements were carried out in the X-ray absorption fine structure (EXAFS) and X-ray absorption near edge spectroscopy (XANES) regions, respectively, located in the Ce L3- and Fe K-edges. The XAFS2 beamline at the Brazilian Synchrotron Light Laboratory (LNLS) was used. XAS spectra were measured at room temperature in the transmission and fluorescence modes, and the energy was calibrated using standard Cr and Fe foils, respectively. More details of the beamline used can be obtained from Ref. 18. The data were analyzed using the Athena and Artemis interfaces.[19]

RESULTS AND DISCUSSION

Figure 1 shows the TGA curve obtained during the synthesis of undoped ceria NPs. Three distinct weight-loss steps are distinguished: (i) the first one develops between ∼23 °C and ∼200 °C (∼10% weight-loss), which was related to the elimination of water and trapped solvent; (ii) the second weight-loss step has been assigned to the combustion of organic residues and develops between ∼200 °C and ∼340 °C (∼60% weight-loss), and (iii) the third step, running from

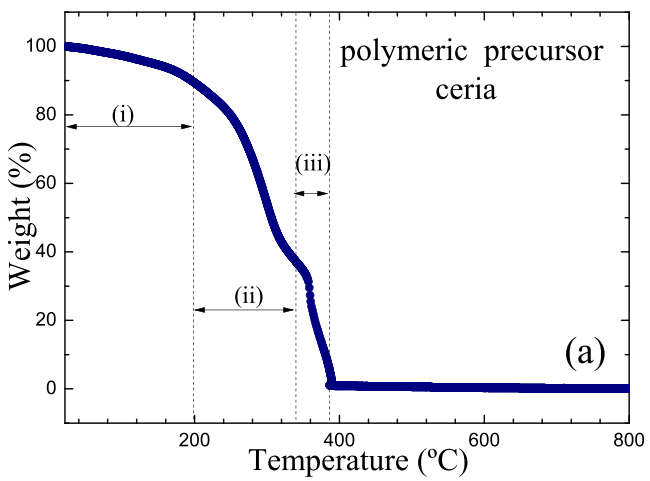

FIG. 1. TGA curve obtained during the synthesis of undoped ceria NPs.

~340 °C to ~390 °C, occurs due to the formation of stable ceria NPs. Above ~390 °C, an important improvement in crystallinity has been achieved. XRD data analysis indicates the formation of pure ceria (fluoride-like structure) crystalline phase (JCPDS card: 34-394) for all synthesized samples, with no evidence of any other crystalline or amorphous impurity phase, within the resolution limit of our instrument. Likewise, we have found the linewidth (FWHM) of the XRD peaks increasing with the Fe content, as observed in Fig. 2(a). This finding correlated with the decrease in the mean particle size and/or with the change in the mean residual strain. In order to obtain further structural information, XRD patterns were analyzed using the Rietveld refinement method. The Rietveld refinement obtained for the undoped ceria NPs is shown in Fig. 2(b).

Table I listed the structural parameters determined from the Rietveld refinement. As can be observed in Table I, the mean lattice constant $\langle a \rangle$ of the undoped ceria sample (5.4065 Å) is close to the reported value of bulk ceria (5.4111 Å). However, as the Fe-content increases, the lattice constant of the doped ceria shows a clear decreasing tendency. This finding has been assumed as a strong evidence of the substitutional solution (solid solution) of cerium-ions and iron-ions in the ceria structure. This result is also supported by the fact that the ionic radii of Fe^{3+}-ions (0.55 Å or 0.645 Å for low or high spin state, respectively) and Fe^{4+}-ions (0.585 Å) are smaller than the ionic radius of Ce^{4+}-ions (0.87 Å), considering a fourfold coordination number.[20] Furthermore, the $\langle D \rangle$ value shows a monotonic decreasing trend as the Fe-content increases [see Fig. 2(c)]. This result has been assigned to the effect of the iron-ions segregation on the particles surface, which reduces the surface energy and leads to a decrease in the mean crystallite size. This finding is in agreement with other works reported in the literature.[14,21–23]

TABLE I. Parameters obtained from the Rietveld refinement of the XRD patterns: mean lattice constant $\langle a \rangle$, mean crystallite size $\langle D \rangle$, and mean residual strain $\langle \varepsilon \rangle$. The S (Rwp/Rexpected) values represented the goodness of the Rietveld refinements. The Fe-content (mol. %) determined from the EDX measurements include numbers between parentheses representing the uncertainties in the last significant digit.

Fe-content (mol. %)	EDX (mol. %)	$\langle a \rangle$ (Å)	$\langle D \rangle$ (nm)	$\langle \varepsilon \rangle$ (%)	S (-)
0	…	5.4065	13.8 ± 1.0	0.087	0.92
1.0	…	5.4060	8.8 ± 1.0	0.235	1.19
2.5	…	5.4044	6.2 ± 1.0	0.324	0.68
5.0	6(1)	5.4035	5.6 ± 1.0	0.446	0.69
7.5	7(1)	5.4037	5.1 ± 1.0	0.483	0.90
10.0	9(1)	5.4013	4.7 ± 1.0	0.538	0.96

Moreover, the reduction of $\langle D \rangle$ values with the increase in Fe content [see Fig. 2(c)] is accompanied by a remarkable increase in the residual strain (see Table I), which is assigned to lattice distortions induced by the entrance of iron-ions. In order to corroborate the mean crystallite size, HRTEM images were obtained. Figure 3(a) shows the HRTEM micrograph of the 5 mol. % iron-doped CeO_2, with its corresponding particle size histogram, which is well modeled by a lognormal distribution function. The mean particle size can be estimated by using the relation: $\langle D \rangle_{MET} = D_o \exp(\sigma^2/2)$, where D_o is the median value and σ is the polydispersion parameter. The values found for $\langle D \rangle_{MET}$ is 6.1 ± 0.2 nm, which is in good agreement with the mean crystalline size (see Table I). The selected area electron diffraction (SAED) pattern recorded from a set of nanoparticles is shown in Fig. 3(b) and reveals three bright rings corresponding to d-values of 0.301, 0.260, and 0.185 nm expected for the (111), (200), and (220) diffraction planes of the CeO_2 structure.

Figure 4(a) shows the room-temperature Raman spectrum of the as-prepared undoped ceria NPs in the range of

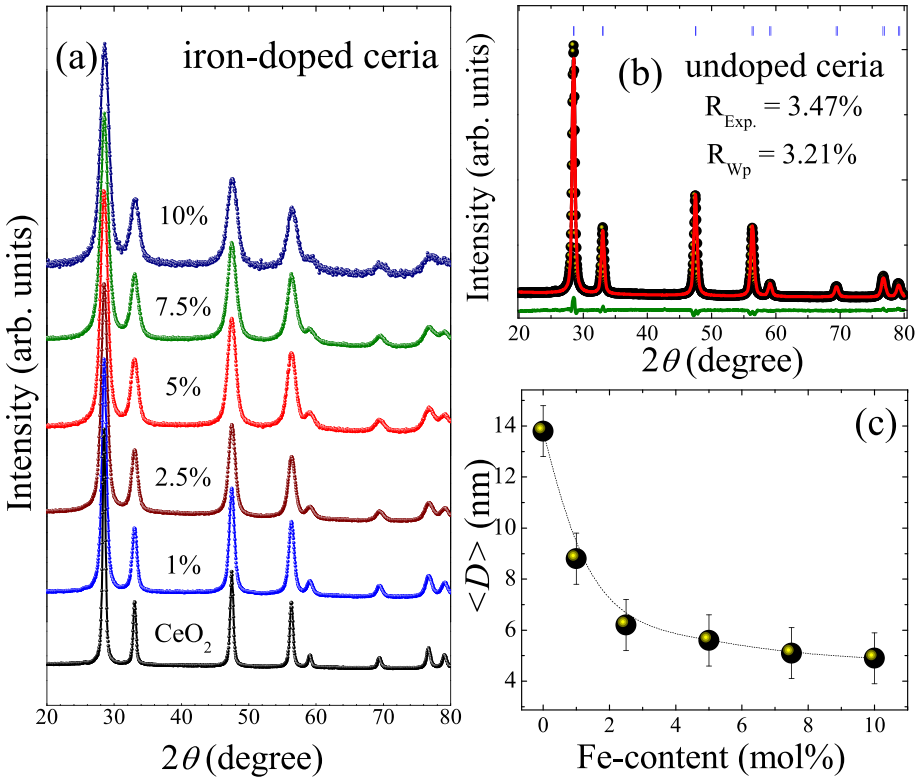

FIG. 2. (a) XRD patterns of undoped and iron-doped ceria NPs. (b) XRD pattern of undoped ceria NPs plus Rietveld refinement, where the experimental data are represented by symbols, calculated data represented by the solid red-line and the difference between experimental and calculated data points represented by the solid green-line. (c) The mean crystallite size as a function of the Fe-content obtained from the Rietveld refinement.

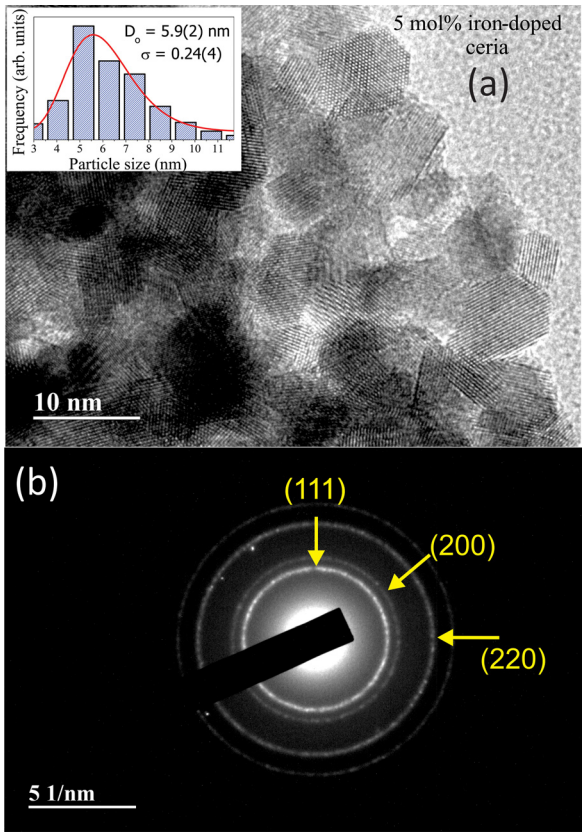

FIG. 3. (a) HRTEM image of Ceria nanoparticles doped with 5 mol. % with their corresponding particle size histograms (the red solid lines represent the log-normal function). (b) HRTEM selected area electron diffraction (SAED).

200–750 cm^{-1}. The spectrum exhibits a broad and asymmetric peak located at ~460 cm^{-1}, which was assigned to the F_{2g} mode. In addition, two side peaks have been observed: (i) the first one located at ~256 cm^{-1} was attributed to the 2TA mode, which is inactive in a perfect ceria crystal,[24] and (ii) the second peak located at ~590 cm^{-1} was associated with oxygen vacancy.[25] As shown in Fig. 4(b), the quenching of the two side peaks after thermal treatment at 900 °C for 2 h has been assigned to the crystallinity improvement, which is evidenced by a remarkable reduction of the linewidth and asymmetry of the main peak.[24] This result is in agreement with the XRD data analysis and indicates an increase from ~13.8 nm to ~44 nm after the thermal treatment. Furthermore, it is observed [see Fig. 4(c)] that the Fe doping of ceria leads to changes in the Raman spectra: (i) a blue shift of the main peak (F_{2g}) from ~460 cm^{-1} to ~465 cm^{-1}, (ii) a clear reduction of the linewidth of the main peak, and (iii) the quenching of the peaks at ~256 cm^{-1} and ~590 cm^{-1} in comparison to that observed for the as-prepared ceria NPs [see Fig. 4(a)]. These features suggest a likely annihilation of defects (oxygen vacancies) with the Fe doping, which was related to the segregation process of the dopant at the particles' surface.[22]

Figure 5(a) shows the temperature (T) dependence of the magnetic susceptibility (χ) of the undoped and iron-doped ceria NPs measured with a DC field of 5 kOe (data are presented after subtracting the signal from the sample holder signal). As observed in Fig. 5(a), the χ vs T curves for the undoped and in the iron-doped ceria NPs show a hyperbolic trend, in the temperature range from 5 K to 300 K, indicating a paramagnetic behavior. The hyperbolic behavior observed for the undoped CeO_2 NPs suggests the presence of a small fraction of Ce^{3+} ions coexisting with Ce^{4+} ions in the CeO_2 hosting matrix. The χ versus T curves have been well modeled with a modified Curie-Weiss law given by $\chi = C/(T - \theta) + \chi_0$, where χ_0 represents a temperature-independent contribution, θ is the Curie-Weiss temperature, and C is the Curie constant ($C = N\mu^2_{eff}/3k_B$, where N is the number of magnetic ions and μ_{eff} is the effective magnetic moment). Table II shows the parameters obtained from the fits of the χ versus T curves. Using the χ versus T curve for the undoped ceria NPs [see inset of Fig. 5(a)] and assuming that the effective magnetic moment of Ce^{3+} ions is $\mu_{eff} = 2.54\ \mu_B$, the estimated amount of Ce^{3+} ions showing a paramagnetic behavior was ~9%. This value is larger than the value reported by Coey *et al.* (~0.4%).[8] The larger amount of Ce^{3+} ions determined in

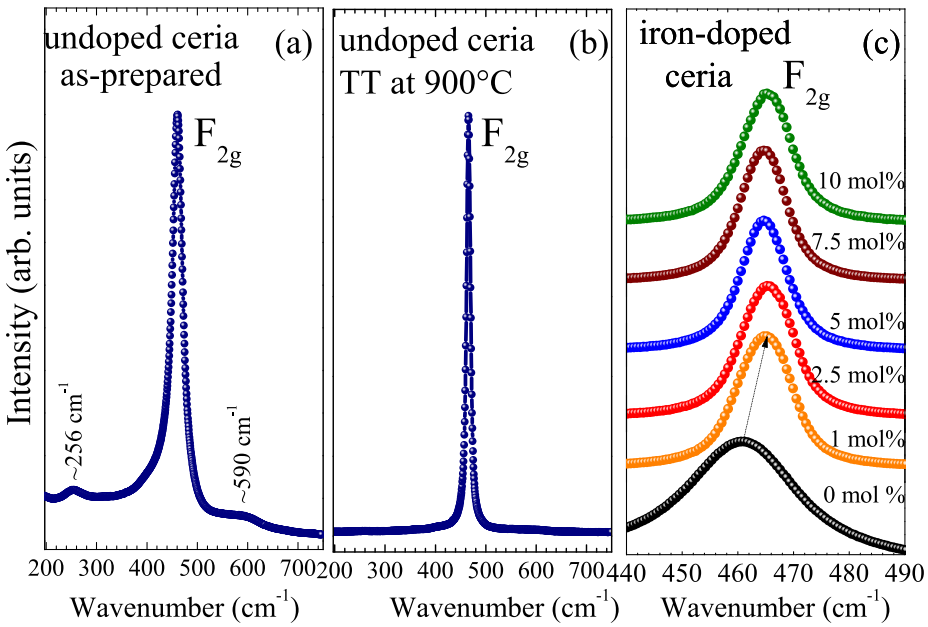

FIG. 4. Room temperature Raman spectra obtained for the undoped ceria NPs: (a) as-prepared and (b) thermally treated (TT) sample at 900 °C during 2 h under air atmosphere. (c) Raman spectra obtained for the iron-doped ceria NPs.

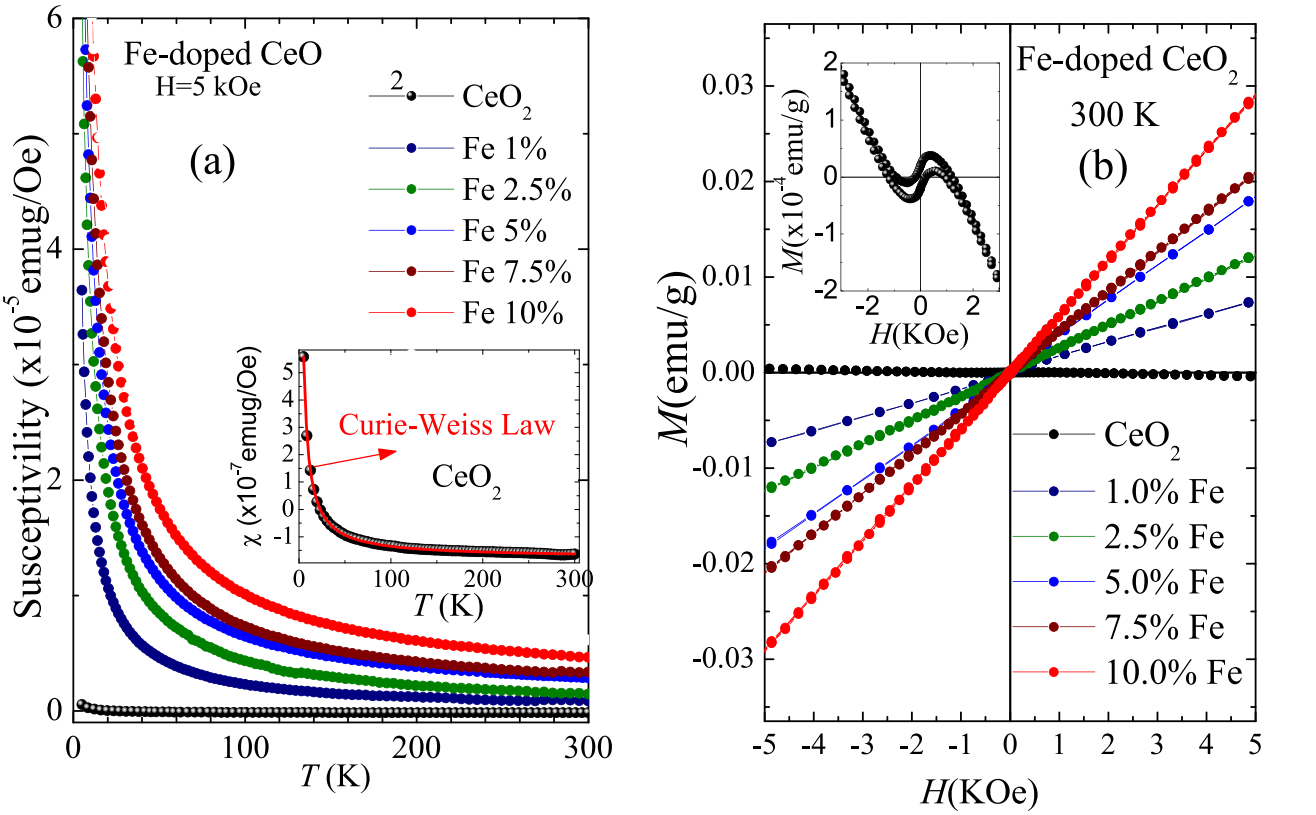

FIG. 5. (a) Curves of magnetic susceptibility (χ) versus temperature (T) of the undoped and iron-doped ceria NPs with a DC field of 5 kOe. The inset displays the fit (red line) of χ versus T curve using the Curie-Weiss law. (b) Room-temperature magnetization (M) versus applied magnetic field (H) of the undoped and iron-doped ceria NPs. The inset shows the magnification of the M *vs* H of the undoped ceria NPs.

our sample could be associated with different methods of synthesis used in this study. With respect of the Fe-doped ceria NPs, the value of C increases as the Fe content increases. An effective magnetic moment of $\mu_{\text{eff}} = 5.61\ \mu_B$ has been obtained for the 1 mol. % iron-doped ceria NPs. This value is close to the spin-only contribution of free Fe^{3+} ions (5.9 μ_B). However, the value of μ_{eff} shows a monotonic reduction from 5.61 μ_B down to 3.28 μ_B as the Fe-content increases from 1 to 10 mol. %. The analysis of XANES data obtained from the iron-doped ceria NPs reveals the presence of only Fe^{3+} ions. This finding is also in agreement with the analysis obtained from the Mössbauer spectra (at room temperature and 20 K) for the 10 mol. % iron-doped sample (Fig. 6), as the Mossbauer spectra is well-resolved by using a doublet. The presence of only doublet excludes the presence of magnetic interactions which is consistent with the paramagnetic behaviour determined from the temperature dependence of the DC susceptibility. The fit provides an isomer shift (IS) value at RT (20 K) of 0.24 mm s^{-1} (0.35 mm s^{-1}) and a quadrupole splitting (QS) at RT (20 K) of 0.95 mm s^{-1} (0.97 mm s^{-1}). These hyperfine parameters are consistent with the presence of only Fe^{3+} ions.[11] These results exclude the presence of iron ions in lower valence states. In order to explain the monotonic reduction of μ_{eff} (see Table II) with the Fe content, the antiferromagnetic (AFM) interaction between Fe^{3+}(Ce^{3+}) and Fe^{3+} mediated by oxygen ions cannot be invoked because in the ceria structure the Ce-O-Ce(Fe) bond angle is ~90°–110°,

TABLE II. Parameters obtained from the fits of χ versus T curves of undoped and iron-doped ceria NPs using the Curie-Weiss law.

x (mol. %)	C ($\times 10^{-5}$ emuK/gOe)	μ_{eff} (μ_B)	θ (K)	χ_0 ($\times 10^{-7}$ emu/gOe)	x_{HS}/x
0	0.42	…	−0.7	−1.8	…
1.0	23	5.61	−1.3	0.8	0.89
2.5	41	4.72	−1.7	2.6	0.60
5.0	51	3.70	−1.9	13.4	0.33
7.5	62	3.31	−2.2	13.0	0.25
10.0	82	3.28	−3.1	20.5	0.24

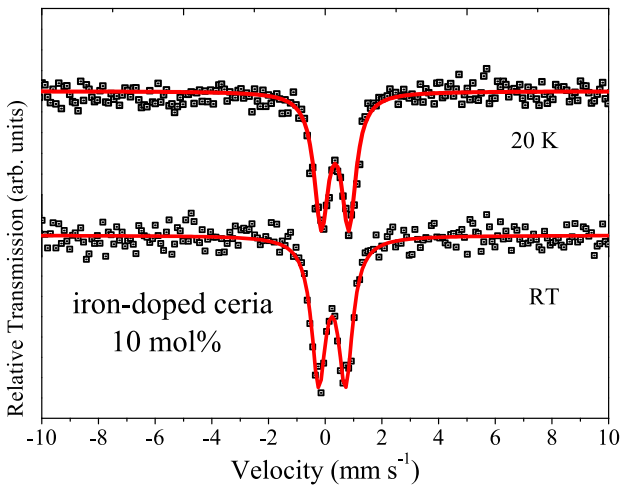

FIG. 6. Mössbauer spectra of 10 mol. % Fe-doped CeO_2 sample recorded at room-temperature and 20 K.

which favors the FM coupling instead.[26] Although the double-electron occupied oxygen vacancies (F^0 centers) can mediate the AFM interactions[27,28] between Fe^{3+}/Fe^{3+} or Fe^{3+}/Ce^{3+}, it implies in having an increased amount of oxygen vacancies with the Fe content, which is not observed in the studied samples. Therefore, a possible explanation can be based on the coexistence of a high-spin ($\mu_{eff} = 5.92\,\mu_B$) and low-spin ($\mu_{eff} = 1.73\,\mu_B$) states of Fe^{3+} ions. It implies that the decreasing tendency of the μ_{eff}/Fe-ion comes from the change of the population of Fe^{3+} ions showing a high-spin state to a low-spin state as the Fe content is increased. A similar tendency has been reported in the literature.[29] Although the origin of this induced spin-state change is unknown, it seems to be related to the augment of local distortions in sites occupied by the iron ions in the ceria matrix. Using the Curie constant obtained from the fits of the χ versus T curves and the μ_{eff} for the low-spin ($1.73\,\mu_B$) and high-spin state ($5.92\,\mu_B$) of Fe^{3+} ions, we estimated the ratio of the iron ions in the high-spin state (x_{HS}/x, where x is the nominal iron concentration) and the values are listed in Table II.

Figure 5(b) shows the room-temperature magnetization (M) versus the applied magnetic field (H) for the undoped as well as for iron-doped ceria NPs. As observed, the M versus H curve displayed for the undoped ceria NPs (300 K) shows a weak ferromagnetism (FM) behavior, with saturation magnetization M_S $\sim 1.8 \times 10^{-4}$ emu/g, which coexist with a diamagnetic signal coming from the nonmagnetic contribution of the ceria matrix. The coercive magnetic field ($H_C \sim 200$ Oe) observed in the hysteresis loop is in agreement with those reported in the literature:[30,31] That the FM contribution can be assigned mainly to the formation of bound magnetic polarons related to the presence of intrinsic defects (oxygen vacancies) and magnetic ions (Ce^{3+}).[9,28] However, the ferromagnetic contribution coming from the Ce^{3+}-O-Ce^{3+} superexchange cannot be ruled out, once the presence of oxygen vacancies would reduce the Ce-O-Ce bond angle in the CeO_2 matrix (in ideal CeO_2 crystal is 109°), as suggested by Peng *et al.*[26]

On the other hand, after the iron doping, the weak FM signal of the undoped ceria NPs has been completely quenched and only paramagnetic behavior is determined. This fact is intriguing, since the remaining of the FM contribution after the Fe doping is reported.[26] The disappearance of the FM signal in the studied Fe doped ceria NPs was assigned to the progressive enrichment of iron dopants at the particles' surface,[14,21] which would drive to the reduction of the oxygen vacancies population. This result is consistent with the extinction of the Raman peak [see Fig. 4(c)] associated with the oxygen vacancies, even when the mean particle size decreases to ~5 nm for the 1% Fe-doped sample in comparison to the undoped one.

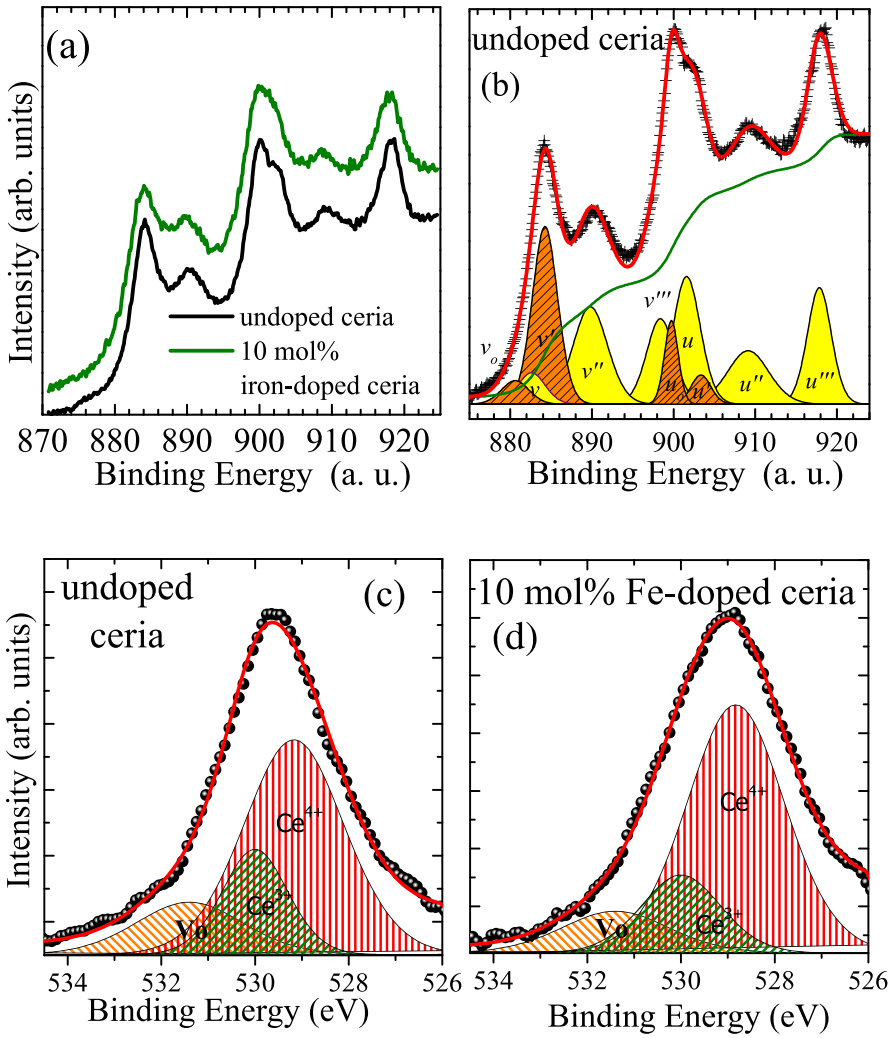

FIG. 7. (a) Ce 3d core level XPS spectra of the undoped and 10 mol. % iron-doped ceria NPs. (b) Deconvolution of the Ce 3d region for the undoped ceria NPs; symbols represented observed data (Obs.) and solid red-line represented calculated data (Cal.). Dashed-orange peaks and yellow peaks are assigned to Ce^{3+} and Ce^{4+} contributions, respectively. O 1s core level XPS spectra of (c) the undoped ceria NPs and (d) the 10 mol. % iron-doped ceria NPs.

TABLE III. Binding energies and integrated peak areas of Ce 3d core level determined for the undoped and 10 mol. % iron-doped ceria NPs.

Fe-content (%)	Ce^{4+}						Ce^{3+}				
	v	v''	v'''	u	u''	u'''	v_o	v'	u_o	u'	$[Ce^{3+}]/[Ce^{3+}+Ce^{4+}]$
0	883.5	891.1	898.4	901.8	908.9	917.9	880.9	884.9	899.9	903.0	0.24
10	883.2	890.7	898.2	901.8	908.7	917.6	880.9	884.7	899.9	903.6	0.21

Figure 7(a) shows the Ce 3d core level XPS measurements of the undoped and 10 mol. % iron-doped ceria NPs. In order to determine the oxidation state of cerium-ions, the deconvolution of the complex Ce 3d structure has been given by ten peaks ($v_o \cdots v'''$, $u_o \cdots u'''$), according to Burroughs *et al.* nomenclature.[32] Although the v, v'', and v''' (u, u'', and u''') peaks represent the Ce $3d_{5/2}$ (Ce $3d_{3/2}$), three final states of Ce^{4+}-ions the v_o and v' (u and u') peaks characterize the Ce $3d_{5/2}$ (Ce $3d_{3/2}$) final state of Ce^{3+}-ions. In order to calculate the relative Ce^{3+}-ions concentration, the ratio equation has been used:[33] $[Ce^{3+}]/[Ce^{3+}+Ce^{4+}] = [\text{area}(v_o, v', u_o, u')]/[\text{total area}]$. The spectra analyses were carried out using the Shirley-type background function and the Gaussian/Lorentzian line shape, and also the branching ratio was fixed to 2/3 to the $v_o/u_o \ldots v'''/u'''$. In Fig. 7(b), a typical fitting is shown. The peaks' positions obtained from the spectra analyses are listed in Table III. The peaks' positions obtained for the undoped ceria NPs are in agreement with the literature.[34] The Ce^{3+}-ion concentration shows a decreasing tendency as the Fe-content increases, evidencing that the entrance of the iron-ions into the matrix drives to a reduction of the Ce^{3+}-ion population, especially on the particle surface. On the other hand, Figs. 7(c) and 7(d) show the deconvolution of the O 1s core level for the as-prepared undoped and 10 mol. % iron-doped nanosized ceria, respectively. The XPS peaks located at 529 eV and 530.0 eV reveal the structural oxygen species associated with CeO_2 and Ce_2O_3, respectively. Meanwhile, the peak located at 531.4 eV has been attributed to oxygen vacancy.[35] A clear spectral area ($Ce^{3+}/Ce^{3+}+Ce^{4+}$) reduction (from ~0.24 to ~0.20) of the peak assigned to oxygen species and related to Ce^{3+}-ions has been observed as the iron-ion is introduced into the hosting matrix. This result suggests the decrease of the Ce^{3+}-ion population in accordance with the analysis of the Ce 3d core level. As the Fe-content increases, the reduction of the spectral area (from ~0.17 to ~0.13) of the peak assigned to oxygen vacancy (Vo) has also been observed, which is in accordance with the quenching of the peak assigned to Vo in the Raman spectra (as discussed earlier), likely due to surface segregation of the dopant-ions as already reported in the literature.[21,22] Figure 8(a) shows the Ce L_3-edge XANES spectra of commercial cerium (IV) oxide and cerium (III) acetate hydrate. The XANES spectrum of cerium (IV) shows two peaks located at ~5731 eV and ~5738 eV whereas for cerium (III) one XANES peak at ~5727 eV. These positions are taken as fingerprints and used herein to determine the oxidation state of cerium-ions. Figure 8(b) shows the Ce L_3-edge XANES spectra of the undoped and iron-doped ceria NPs. The spectra obtained for the undoped ceria NPs after the thermal treatment (900 °C) is also included in Fig. 8(b). A visual inspection of the spectra's shape suggests that only Ce^{4+}-ions are present in all synthesized samples. However, using a deconvolution of the recorded spectra, the presence of Ce^{3+}-ions was assessed, as already reported in the literature.[36,37] In this regard, the spectra's fit, using three peaks instead of two, has been carried out: one component related

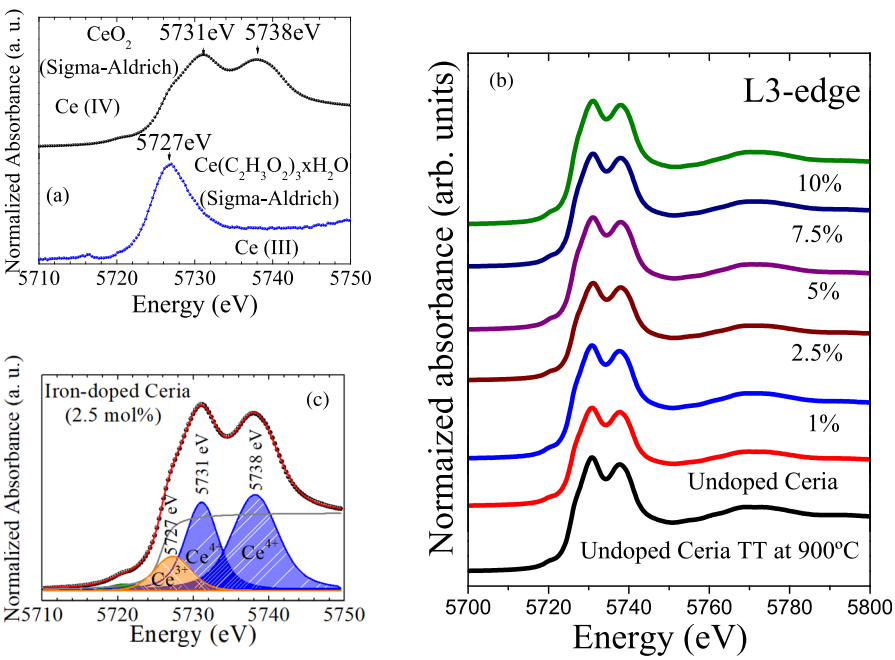

FIG. 8. Room-temperature Ce L3-edge XANES spectra obtained for (a) commercial cerium (IV) oxide and cerium (III) acetate hydrate; (b) undoped and iron-doped ceria NPs; and (c) fit of the XANES spectrum of the 2.5 mol. % iron-doped ceria NPs using three components.

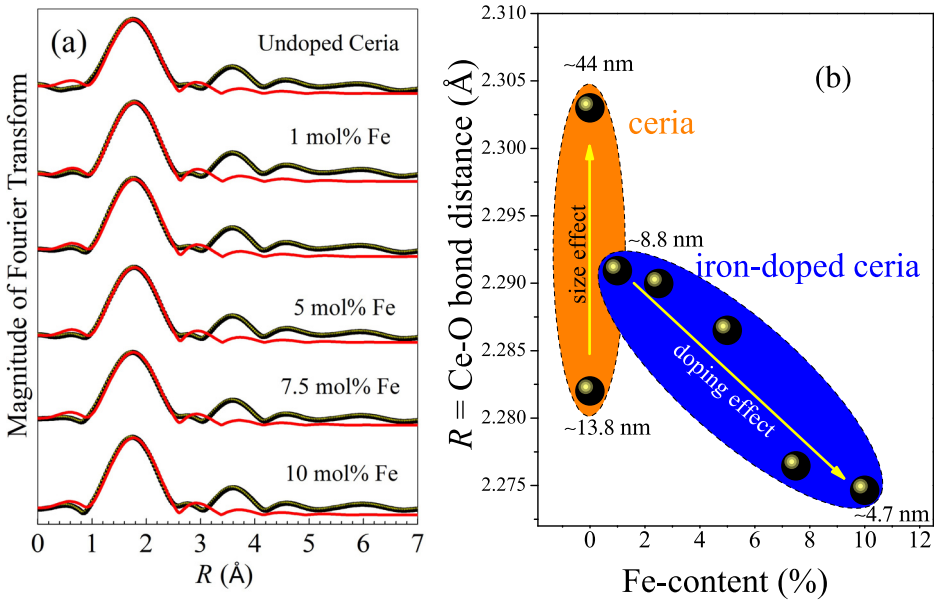

FIG. 9. (a) Fourier-transformed amplitude of EXAFS at the Ce L3-edge for the undoped (as-prepared) and iron-doped ceria NPs. (b) Evolution of the bond distance (Ce-O) as the size effect (orange) and doping effect (sky blue).

to Ce^{+3}-ions (located at 5727 eV) and two components related to Ce^{4+}-ions (located at 5731 and 5738 eV). A typical fit obtained for the 2.5 mol. % iron-doped ceria NPs is shown in Fig. 8(c). The estimation of the Ce^{3+}-content for the undoped ceria NPs has been obtained using the spectral area ratio of the peaks $[Ce^{3+}/(Ce^{3+}+Ce^{4+})]$. Our finding for the undoped ceria NPs shows a Ce^{3+}-content of ∼10%, which is lower than the content assessed from magnetic measurements. One likely explanation for this deviation is that only a fraction of the Ce^{3+}-ions shows paramagnetic behavior.

A similar analysis is carried out for all iron-doped samples, which indicates no clear change in the Ce^{3+}-content as the Fe-content increases. Meanwhile, the short-range ordered structure surrounding the cerium-ions is investigated via the Ce L_3-edge extended X-ray absorption fine structure (EXAFS) data. Figure 9(a) shows the Fourier transforms of the undoped and iron-doped ceria NPs. We have observed that all samples show similar shapes, suggesting similar crystal environment for the cerium-ions. Furthermore, the cubic fluorite-type structure is used to model the EXAFS's spectra, including only the first shell [see the red solid-line in Fig. 9(a)]. A bond distance of ∼2.282 Å is determined for the undoped ceria NPs, whereas this distance increases to ∼2.303 Å after thermal treatment at 900 °C for 2 h, which was associated with the size increase of the particles. The assessed value is close to the bulk value of ceria (2.343 Å).[38] With respect to the iron-doped ceria NPs, we have found a regular trend of the bond distance, as showed in Fig. 7(b). The Ce-O bond distance tends to decrease monotonically as the Fe-content increases. This decreasing tendency evidences the substitutional solution regime in agreement with the XRD data analysis discussed earlier.

Figures 10(a) and 10(b) show the Fe K-edge XANES and EXAFS spectra obtained for the iron-doped ceria NPs. α-Fe_2O_3 and FeO bulk samples were used as references.

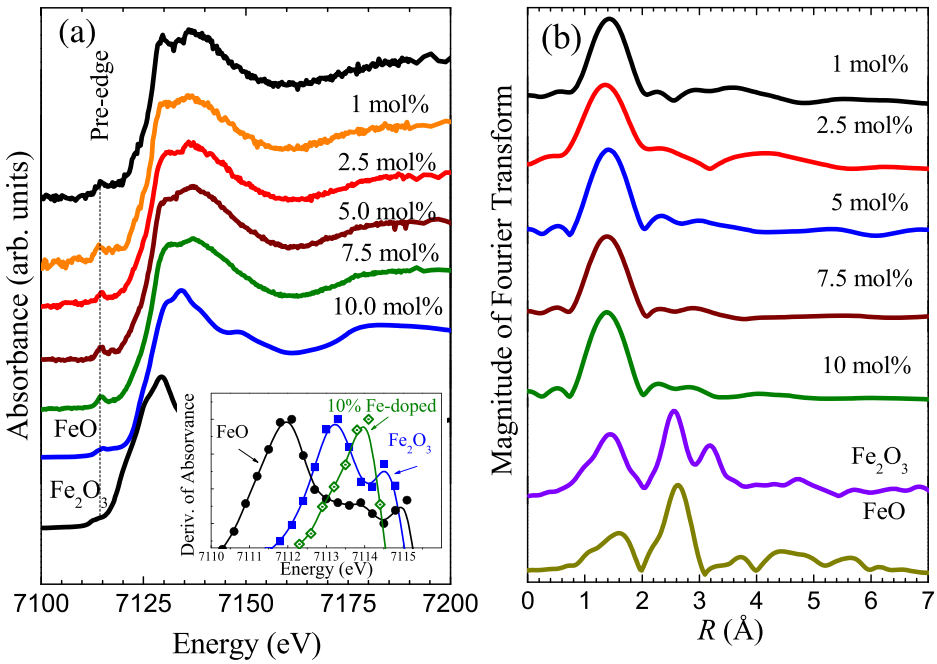

FIG. 10. (a) Fe K-edge XANES spectra of the iron-doped ceria NPs. XANES spectra obtained for α-Fe_2O_3 and FeO are included as references. The inset in (a) showed the first-order derivative of the normalized absorbance curves around the pre-edge peaks of the reference samples (α-Fe_2O_3 and FeO) and for the 10 mol. % iron-doped ceria NPs. (b) Fourier-transform amplitude of the Fe K-edge EXAFS spectra.

According to the literature, the pre-edge peaks are positioned at ∼7112 eV and ∼7114 eV for Fe^{2+}- and Fe^{3+}-ions, respectively.[39] Then, the pre-edge peak position determined from the spectra of the iron-doped ceria NPs has been used to determine the oxidation state of the iron-ions. The inset of Fig. 10(a) shows the first-order derivative of the normalized absorbance curves obtained for the 10 mol. % iron-doped ceria NPs and references (α-Fe_2O_3 and FeO). Using the maximum to represent the pre-edge peak,[39] the iron-doped ceria NPs shows a maximum at ∼7114 eV, which is around the maximum observed for the reference sample containing only Fe^{3+}-ions (α-Fe_2O_3). Similar results were obtained for all studied samples, suggesting a valence state of 3+ for the iron ions in the iron-doped ceria NPs.

On the other hand, with respect to the spectra of the reference samples (α-Fe_2O_3 and FeO), clear differences are observed in the EXAFS spectra of the iron-doped ceria NPs, allowing us to rule out the presence of iron oxide phases. Meanwhile, the Fe K-edge EXAFS spectra of the iron-doped ceria NPs show similar shapes to that obtained from the Ce L_3-edge EXAFS spectra, as shown in Fig. 10(a). This result suggests the same coordination number for iron- and cerium-ions, reinforcing the substitutional solution regime of iron and cerium ions within the iron-doped ceria matrix, in agreement with that reported by Wang *et al.*[10]

CONCLUSIONS

Undoped and iron-doped (0–10 mol. %) single-phased ceria nanoparticles with a high crystallinity have been successfully synthesized by a polymer precursor method. A mean crystallite size of ∼13.8 nm has been determined for the undoped ceria nanoparticles. Meanwhile, a mean size of ∼4.5 nm was determined for the 10 mol. % iron-doped ceria nanoparticles, which reveals a monotonous reduction in the mean crystallite size as the iron-doping content increases. Room ferromagnetism associated with oxygen vacancies, which mediate the bound magnetic polarons of Ce^{3+} has been determined for the undoped sample. Meanwhile, at low temperatures, the thermal dependence of the susceptibility suggests the occurrence of paramagnetism assigned to some Ce^{3+} ions, which do not participate in the oxygen-vacancies mediated ferromagnetism observed at room temperature. The presence of Ce^{3+} coexisting with Ce^{4+} has been determined from the Ce L3-edge XANES data analysis. That coexistence seems to occur at the particles surface due to the lower coordination number, which favors the generation of oxygen vacancies, as evidenced by Raman and XPS spectroscopy measurements. The magnetic measurements of the iron-doped samples are consistent with a paramagnetic behavior of the Fe^{3+} ions. A reduction of the effective magnetic moment of the Fe^{3+} ions is observed, and it was interpreted due to the change from a high-spin to low-spin state of Fe ions as the Fe content is increased. The presence of only Fe^{3+} ions in all samples is determined from the Fe K-edge XANES data analysis in agreement with Mössbauer spectroscopy results and magnetic measurements. The reduction of the unit cell volume concomitantly with the shortening of the Ce-O bond distances as the Fe content increases suggests the substitutional solution of cerium and iron ions in the cation sites of the fluorite structure. Within the limit of detection of our experimental techniques, the absence of a dopant segregation phase corroborates the substitutional solution regime.

ACKNOWLEDGMENTS

This work was financially supported by the Brazilian agencies CNPq, CAPES, and FAPDF. The authors thank the Brazilian Synchrotron Light Laboratory (LNLS) for the beamtime granted (proposal 20160072) to carry out the X-ray absorption measurements. The authors would like to thank Dr. E. Guimarães for her help with the X-ray diffraction experiments.

[1]H. C. Yao and Y. F. Y. Yao, J. Catal. **86**, 254 (1984).
[2]J. Kašpar, P. Fornasiero, and M. Graziani, Catal. Today **50**, 285 (1999).
[3]H. W. Jen, G. W. Graham, W. Chun, R. W. McCabe, J. P. Cuif, S. E. Deutsch, and O. Touret, Catal. Today **50**, 309 (1999).
[4]Z. Liao, P. Gao, Y. Meng, W. Fu, X. Bai, H. Zhao, and D. Chen, Solid-State Electron. **72**, 4 (2012).
[5]L. Liao, H. X. Mai, Q. Yuan, H. B. Lu, J. C. Li, C. Liu, C. H. Yan, Z. X. Shen, and T. Yu, J. Phys. Chem. C **112**, 9061 (2008).
[6]S. Park, J. M. Vohs, and R. J. Gorte, Nature **404**, 265 (2000).
[7]S. Banerjee, M. Mandal, N. Gayathri, and M. Sardar, Appl. Phys. Lett. **91**, 182501 (2007).
[8]M. Coey, K. Ackland, M. Venkatesan, and S. Sen, Nat. Phys. **12**, 694 (2016).
[9]A. Sundaresan, R. Bhargavi, N. Rangarajan, U. Siddesh, and C. N. R. Rao, Phys. Rev. B **74**, 161306 (2006).
[10]W.-C. Wang, S.-Y. Chen, P.-A. Glans, J. Guo, R.-J. Chen, K.-W. Fong, C.-L. Chen, A. Gloter, C.-L. Chang, T.-S. Chan, J.-M. Chen, J.-F. Lee, and C.-L. Dong, Phys. Chem. Chem. Phys. **15**, 14701 (2013).
[11]J. M. D. Coey, A. P. Douvalis, C. B. Fitzgerald, and M. Venkatesan, Appl. Phys. Lett. **84**, 1332 (2004).
[12]A. Punnoose, M. S. Seehra, W. K. Park, and J. S. Moodera, J. Appl. Phys. **93**, 7867 (2003).
[13]M. V. Vaishampayan, R. G. Deshmukh, P. Walke, and I. S. Mulla, Mater. Chem. Phys. **109**, 230 (2008).
[14]R. H. R. Castro, P. Hidalgo, R. Muccillo, and D. Gouvêa, Appl. Surf. Sci. **214**, 172 (2003).
[15]R. A. Young, A. Sakthivel, T. S. Moss, and C. O. Paiva-Santos, J. Appl. Crystallogr. **28**, 366 (1995).
[16]P. Thompson, D. E. Cox, and J. B. Hastings, J. Appl. Crystallogr. **20**, 79 (1987).
[17]C. O. Paiva-Santos, A. A. Cavalheiro, M. A. Zaghete, M. Cilense, J. A. Varela, M. T. Silva Giotto, and Y. P. Mascarenhas, Adv. X-Ray Anal. **44**, 38 (2001).
[18]S. J. A. Figueroa, J. C. Mauricio, J. Murari, D. B. Beniz, J. R. Piton, H. H. Slepicka, M. F. d. Sousa, A. M. Espíndola, and A. P. S. Levinsky, J. Phys.: Conf. Ser. **712**, 012022 (2016).
[19]B. Ravel and M. Newville, J. Synchrotron Radiat. **12**, 537 (2005).
[20]R. D. Shannon, Acta Crystallogr., A **32**, 751 (1976).
[21]R. H. R. Castro, P. Hidalgo, J. A. H. Coaquira, J. Bettini, D. Zanchet, and D. Gouvêa, Eur. J. Inorg. Chem. **2005**, 2134.
[22]F. H. Aragón, I. Gonzalez, J. A. H. Coaquira, P. Hidalgo, H. F. Brito, J. D. Ardisson, W. A. A. Macedo, and P. C. Morais, J. Phys. Chem. C **119**(16), 8711 (2015).
[23]H. Coelho-Júnior, J. C. R. Aquino, F. H. Aragón, P. Hidalgo, R. Cohen, L. C. C. M. Nagamine, J. A. H. Coaquira, S. W. da Silva, and H. F. Brito, J. Nanopart. Res. **16**, 2689 (2014).
[24]J. E. Spanier, R. D. Robinson, F. Zhang, S.-W. Chan, and I. P. Herman, Phys. Rev. B **64**, 245407 (2001).
[25]Y. Lee, G. He, A. J. Akey, R. Si, M. Flytzani-Stephanopoulos, and I. P. Herman, J. Am. Chem. Soc. **133**, 12952 (2011).
[26]D.-Z. Peng, S.-Y. Chen, C.-L. Chen, A. Gloter, F.-T. Huang, C.-L. Dong, T.-S. Chan, J.-M. Chen, J.-F. Lee, H.-J. Lin, C.-T. Chen, and Y.-Y. Chen, Langmuir **30**, 10430 (2014).
[27]N. Paunovic, Z. Dohcevic-Mitrovic, R. Scurtu, S. Askrabic, M. Prekajski, B. Matovic, and Z. V. Popovic, Nanoscale **4**, 5469 (2012).

[28]J. M. D. Coey, M. Venkatesan, and C. B. Fitzgerald, Nat. Mater. **4**, 173 (2005).
[29]S. Phokha, S. Pinitsoontorn, and S. Maensiri, Nano-Micro Lett. **5**, 223 (2013).
[30]Y. Liu, Z. Lockmanm, A. Aziz, and J. MacManus-Driscoll, J. Phys.: Condens. Matter **20**, 165201 (2008).
[31]C. Xiaobo, L. Guangshe, S. Yiguo, Q. Xiaoqing, L. Liping, and Z. Zhigang, Nanotechnology **20**, 115606 (2009).
[32]P. Burroughs, A. Hamnett, A. F. Orchard, and G. Thornton, J. Chem. Soc., Dalton Trans. **0**, 1686 (1976).
[33]H. Borchert, Y. V. Frolova, V. V. Kaichev, I. P. Prosvirin, G. M. Alikina, A. I. Lukashevich, V. I. Zaikovskii, E. M. Moroz, S. N. Trukhan, V. P. Ivanov, E. A. Paukshtis, V. I. Bukhtiyarov, and V. A. Sadykov, J. Phys. Chem. B **109**, 5728 (2005).
[34]M. Romeo, K. Bak, J. E. Fallah, F. L. Normand, and L. Hilaire, Surf. Interface Anal. **20**, 508 (1993).
[35]S. A. Ansari, M. M. Khan, M. O. Ansari, S. Kalathil, J. Lee, and M. H. Cho, RSC Adv. **4**, 16782 (2014).
[36]S. Phokha, S. Pinitsoontorn, and S. Maensiri, Nano-Micro Lett. **5**, 223 (2013).
[37]V. Fernandes, I. L. Graff, J. Varalda, L. Amaral, P. Fichtner, D. Demaille, Y. Zheng, W. H. Schreiner, and D. H. Mosca, J. Electrochem. Soc **159**, K27 (2011).
[38]Z. Wu, J. Zhang, R. E. Benfield, Y. Ding, D. Grandjean, Z. Zhang, and X. Ju, J. Phys. Chem. B **106**, 4569 (2002).
[39]M. Wilke, F. Farges, P.-E. Petit, G. E. Brown, and F. Martin, Am. Miner. **86**, 714 (2001).